Check for updates

Quasi-2D Lead–Tin Perovskite Memory Devices Fabricated by Blade Coating

*Lijun Chen, Jun Xi, Eelco Kinsa Tekelenburg, Karolina Tran, Giuseppe Portale, Christoph J Brabec, and Maria Antonietta Loi**

Two terminal passive devices are regarded as one of the promising candidates to solve the processor-memory bottleneck in the Von Neumann computing architectures. Many different materials are used to fabricate memory devices, which have the potential to act as synapses in future neuromorphic electronics. Metal halide perovskites are attractive for memory devices as they display high density of defects with a low migration barrier. However, to become promising for a future neuromorphic technology, attention should be paid on non-toxic materials and scalable deposition processes. Herein, it is reported for the first time the successful fabrication of resistive memory devices using quasi-2D tin–lead perovskite of composition $(BA)_2MA_4(Pb_{0.5}Sn_{0.5})_5I_{16}$ by blade coating. The devices show typical memory characteristics with excellent endurance (2000 cycles), retention (10^5 s), and storage stability (3 months). Importantly, the memory devices successfully emulate synaptic behaviors such as spike-timing-dependent plasticity, paired-pulse facilitation, short-term potentiation, and long-term potentiation. A mix of slow (ionic) transport and fast (electronic) transport (charge trapping and de-trapping) is proven to be responsible for the observed resistive switching behavior.

1. Introduction

Two terminal passive devices are regarded as one of the promising candidates for next-generation nonvolatile memory storage to solve the processor-memory bottleneck in the Von Neumann computing architectures.[1,2] In addition, they have also shown the potential to act as artificial synapses in future neuromorphic electronics as they exhibit low power consumption, possibility of high integration density, and fast switching speed.[3,4] In general, these devices have top-electrode/active layer/bottom-electrode structure that works by switching the resistance of the active material between a high resistance state (HRS) and a low resistance state (LRS).[5,6] Among the different materials and different mechanisms that are used in these devices, active materials with high density of defects and low defect migration barrier are proven to be among the most promising for this application.[7]

Metal halide perovskites (MHPs) exhibit excellent optoelectronic properties, but a number of randomly distributed defects (vacancies, interstitial, anti-site substitution, grain boundaries, and dangling bonds) are identified as detrimental for photovoltaic devices, light-emitting diodes, photodetectors, and lasers.[8] Inspired by the defect-induced hysteresis observed in current–voltage characteristics of perovskites solar cells,[9,10] MHPs-based memory devices have recently aroused interest owing to the easy deposition process and intrinsic multi-trap state characteristics.[11,12] 3D organic–inorganic lead MHPs have been extensively studied in resistive switching (RS) devices, but have shown to suffer from inherent toxicity (Pb content), environmental instability, and poor endurance and retention.[13] Therefore, novel perovskites,[14–18]

L. Chen, J. Xi, E. K. Tekelenburg, K. Tran, G. Portale, C. J Brabec, M. A. Loi
Zernike Institute for Advanced Materials
University of Groningen
Nijenborgh 4, Groningen 9747 AG, The Netherlands
E-mail: m.a.loi@rug.nl

The ORCID identification number(s) for the author(s) of this article can be found under https://doi.org/10.1002/smtd.202300040

© 2023 The Authors. Small Methods published by Wiley-VCH GmbH. This is an open access article under the terms of the Creative Commons Attribution-NonCommercial-NoDerivs License, which permits use and distribution in any medium, provided the original work is properly cited, the use is non-commercial and no modifications or adaptations are made.

DOI: 10.1002/smtd.202300040

J. Xi
Key Laboratory for Physical Electronics and Devices of the Ministry of Education & Shaanxi Key Lab of Information Photonic Technique
School of Electronic Science and Engineering
Xi'an Jiaotong University
No.28, Xianning West Road, Xi'an 710049, China

C. J Brabec
Institute of Materials for Electronics and Energy Technology (i-MEET)
Department of Materials Science and Engineering
Friedrich-Alexander-University Erlangen-Nürnberg
Martensstrasse 7, 91058 Erlangen, Germany

C. J Brabec
Helmholtz-Institute Erlangen-Nürnberg (HI ERN)
Immerwahrstraße 2, 91058 Erlangen, Germany

especially the ones generally called 2D and quasi-2D,[19] have been proposed for improving the environmental instability and repeatability. The insertion of large organic spacer cations in the mixture of ions used for the synthesis leads to spontaneous formation of multilayer of octahedra (n), leading to both quantum and dielectric confinement of carriers in the octahedral planes. These structures have been shown to have advantages to the 3D counterparts, such as offering the possibility of modulating the defect density and increased structural stability.[20,21]

In view of their full confinement and the consequent low RS behavior, 2D perovskites are not the ideal candidate for this application. However, quasi-2D MHPs are considered as a potential candidate for combining excellent RS characteristics and improved environmental stability, furthermore, they offer the possibility of manipulating the phase distribution (vide intra). Recently, quasi-2D MHPs phenylethylammonium (PEA) and n-butylammonium (BA)-based memory devices were reported to exhibit unique memory properties and environmental stability when compared with pure 2D ($n = 1$) and 3D materials ($n = \infty$).[22–24] Moreover, quasi-2D MHPs show potential advantages in artificial synapses and accurate image recognition for their low noise and highly-linear synaptic properties.[25,26] However, most of these works use Pb based compounds, while quasi-2D Sn hybrid perovskites are rarely reported, even if they are a more environment-friendly option. Sn displays similar electron configuration of Pb, and Sn-based perovskites are regarded as one of the most promising alternatives as they maintain excellent optoelectronic properties.[27–31] However, pure Sn perovskites still suffer from rapid oxidation under ambient conditions, which is detrimental for device performance. To this end, Pb–Sn binary systems have been proposed to simultaneously achieve higher stability and reduce the Pb impact.[32]

Most MHPs memristors are deposited using lab scale spin-coating, which is a wasteful technique (5–10% utilization of the precursors) that limits the possibility to tune the growth parameters. Therefore, the development of scalable solution deposition techniques, giving a full control on growth mechanism of the active layer, is urgently needed toward potential applications.[33] Blade coating is a facile method that has industrially relevant sister techniques. It is characterized by a very high precursor utilization rate and allows tuning the deposition temperature, which is extremely important for the control of the growth of metal halide perovskites.[34]

In this study, we address the challenges described above by reducing the Pb content without compromising the robustness of the perovskite memory devices. We report the successful development of quasi-2D Pb–Sn perovskites-based RS memory devices by using the scalable blade coating technique. Here, the optimized devices show bipolar resistive memory characteristics with excellent endurance (2000 cycles), retention (10^5 s), and storage stability (3 months). Moreover, the Pb–Sn binary devices successfully emulate synaptic behaviors such as STDP, PPF, STP, and LTP. At last, ionic movement and charge trapping and de-trapping from bulk and surface defects of the metal halide perovskite (electronic transport) are proven to be responsible for the observed resistive switching behaviors.

2. Results and Discussion

The schematic diagram of **Figure 1**a illustrates how the quasi-2D Pb–Sn mixed perovskites are fabricated using a one-step blade-coating process. The whole memory device structure composed of ITO/PEDOT:PSS/$(BA)_2MA_4(Pb_{0.5}Sn_{0.5})_5I_{16}$/PMMA/Au is shown in Figure 1b. The thin PMMA layer prevents the reaction of the perovskite with the top electrode, as well as protects the active layer from moisture and oxygen from the atmosphere. While the insulating layer has little effect on the RS properties of the memory device, it decreases the current level of the HRS.[14] This device structure acts as an artificial variant of the biological synapse, where the top and bottom electrodes act as pre- and post-synaptic neurons, respectively. Large substrates (9 cm^2) with a uniform active layer composing 25 devices are prepared at one time with blade coating. The utilization rate of the precursor solution with blade-coating is as high as 90–95% and compares extremely favorable to the only 5–10% used with spin-coating. In Figure 1c, a typical *J*–*V* curve is presented in semi-logarithmic scale, where the scan is conducted at DC voltage ($0 \rightarrow 2 \rightarrow 0 \rightarrow -2 \rightarrow 0$ V) with rate of 0.04 V ms^{-1} under dark conditions. Reproducible and reliable bipolar RS with ON/OFF ratio of 10^2 is observed for the quasi-2D Sn–Pb perovskite. The devices switch from the HRS to LRS at 1.35 V in forward sweep direction without any electroforming process, when a negative voltage sweep is applied, the device switches back to the LRS, corresponding to a reset process. Additionally, the repeatability of the resistive switching behavior is confirmed in Figure S1a (Supporting Information), suggesting the reversibility and reproducibility of the memory device. We note that in our attempt of obtaining the best performance we compared different compositions, i.e., we exchanged BA with the monovalent organic cations of phenylethylammonium (PEA) and the divalent organic cations of 3-(aminomethyl) piperidinium (3-AMP) as well as pure Sn system (Figure S1b–d, Supporting Information). The experimental results show that the samples that include the aliphatic BA have better switching characteristics than the ones using aromatic cations. In addition, we also confirm that the RS characteristics of the quasi-2D Sn–Pb perovskite are better than those of the equivalent samples made with Sn-only. The top-view scanning electron microscopy (SEM) images of quasi-2D Pb–Sn perovskite are shown in **Figure 2**a, showing that uniform and compact $(BA)_2MA_4(Pb_{0.5}Sn_{0.5})_5I_{16}$ films are obtained with large grain of lateral size of ≈5 µm. The irregular morphology and poor coverage of $(BA)_2MA_4Sn_5I_{16}$ film (Figure S2a, Supporting Information) is one of the reasons for less efficient memory devices when compared to the one using a mixed Pb–Sn composition. Consistent with the SEM results, the surface root mean square (RMS) roughness obtained from atomic force microscopy micrographs (Figure 2b) of the quasi-2D Pb–Sn exhibits a lower roughness of 23.56 nm compared to the 62.5 nm of the pure Sn compound (Figure S2b, Supporting Information).

In Figure 2c and Figure S3a (Supporting Information), the crystallinity of perovskite films is evaluated with X-ray diffraction (XRD). Two dominant reflections are clearly observed at diffraction angles (2θ) of 14.1^o and 28.4^o that correspond to the (101/111) and (202/222) crystal planes of the quasi-2D system, respectively. The stronger intensity and narrower diffraction peak

 © 2023 The Authors. Small Methods published by Wiley-VCH GmbH

23669608, 2024, 2, Downloaded from https://onlinelibrary.wiley.com/doi/10.1002/smtd.202300040 by Forschungszentrum Jülich GmbH Research Center, Wiley Online Library on [28/01/2025]. See the Terms and Conditions (https://onlinelibrary.wiley.com/terms-and-conditions) on Wiley Online Library for rules of use; OA articles are governed by the applicable Creative Commons License

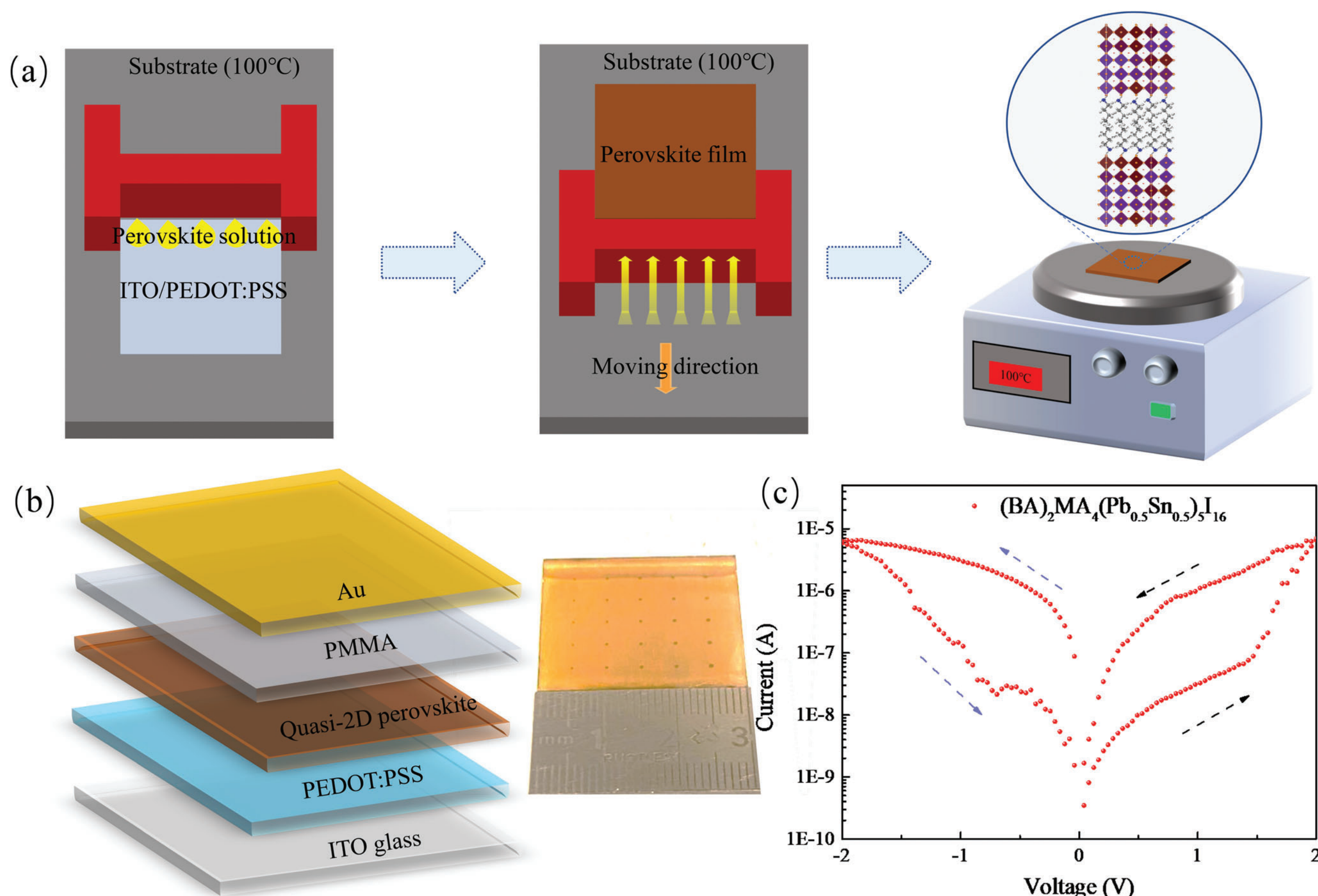

Figure 1. a) Schematic diagram of the perovskite deposition by blade coating (top view). b) Schematic structure of the memristor based on quasi-2D perovskites. Insert: photograph of substrate with 25 memory device. c) *J–V* curve of the devices based on quasi-2D Sn–Pb perovskite.

of the quasi-2D Pb–Sn sample proves better crystallinity than the quasi-2D Sn perovskite (Figure S3a, Supporting Information). The UV–vis absorption spectra (Figure S5, Supporting Information) of the two quasi-2D compounds both show no evidence of excitonic peaks and an absorption edge of 1.23 and 1.38 eV for the Pb–Sn and Sn systems, respectively. Even if is not obvious in the absorption spectra, we find in our XRD experiment (see insert of Figure 2c) that the Pb–Sn system is composed by a mixture of phases corresponding to layered perovskite with n = 1,2,3. In contrast, pure Sn films show a dominant n = 3 phase (Figure S3a, Supporting Information). To further explore structure and orientation of perovskite crystallites in the two systems, grazing incidence wide-angle X-ray scattering (GIWAXS) is conducted, and the results are reported in Figure 2d and Figures S3b and S4 (Supporting Information). Figure 2d and Figure S3b (Supporting Information) show the GIWAXS patterns of the quasi-2D systems. Direct pattern comparison shows a clear tendency for the Pb–Sn system to be more ordered and better oriented than the Sn system, in agreement with the XRD results. While the $BA_2MA_4Sn_5I_{16}$ thin films exhibit mostly diffraction rings with minor presence of arc-like signals, the $(BA)_2MA_4(Pb_{0.5}Sn_{0.5})_5I_{16}$ film shows majority of clearly defined diffraction spots, related to the formation of crystallites with high degree of orientation. Peak assignment of the GIWAXS patterns allows for structure determination of the two systems (Figure S4, Supporting Information). The Sn system shows the predominant presence of the n = 3 phases. The GIWAXS pattern consists of an overlap between slightly anisotropic signals located along the quasi-vertical direction that can be assigned to the 020, 040, 060, 080, 010 and 0160 peaks, indicating the presence of crystallites aligned with the 0k0 planes parallel to the substrates. The most intense isotropic rings can be indexed as the 111/101 and the 202/222 signals for the quasi-2D structure. The derived unit cell for the n = 3 phase is 9 × 9 ×52 Å and Cmce space group, in agreement with literature reports.[35] In agreement with the XRD results, the Pb–Sn film is composed of a mixture of n = 1,2,3 phases, as derived by the assignment of the low angle signals. The observed low angle peaks for all the three phases show strong polarization along the quasi-vertical q_z direction, suggesting high degree of crystallite orientation with the 0k0 planes parallel to the substrate. Some of the well-defined diffraction spots can only be indexed considering the presence of 3D crystallites ($MAPbI_3$ or $MASnI_3$) with slightly distorted tetragonal unit cells with dimensions approximately 9 × 9× 12.6 Å, in agreement with the structure reported in literature for both tetragonal $MAPbI_3$ and $MASnI_3$.[36] Two preferential orientations of the 3D crystallites are observed, with the 101 and 010 planes parallel to the substrate. In summary, the X-ray analysis clearly suggests the existence of multiple phases in

© 2023 The Authors. Small Methods published by Wiley-VCH GmbH

23669608, 2024, 2, Downloaded from https://onlinelibrary.wiley.com/doi/10.1002/smtd.202300040 by Forschungszentrum Jülich GmbH Research Center, Wiley Online Library on [28/01/2025]. See the Terms and Conditions (https://onlinelibrary.wiley.com/terms-and-conditions) on Wiley Online Library for rules of use; OA articles are governed by the applicable Creative Commons License

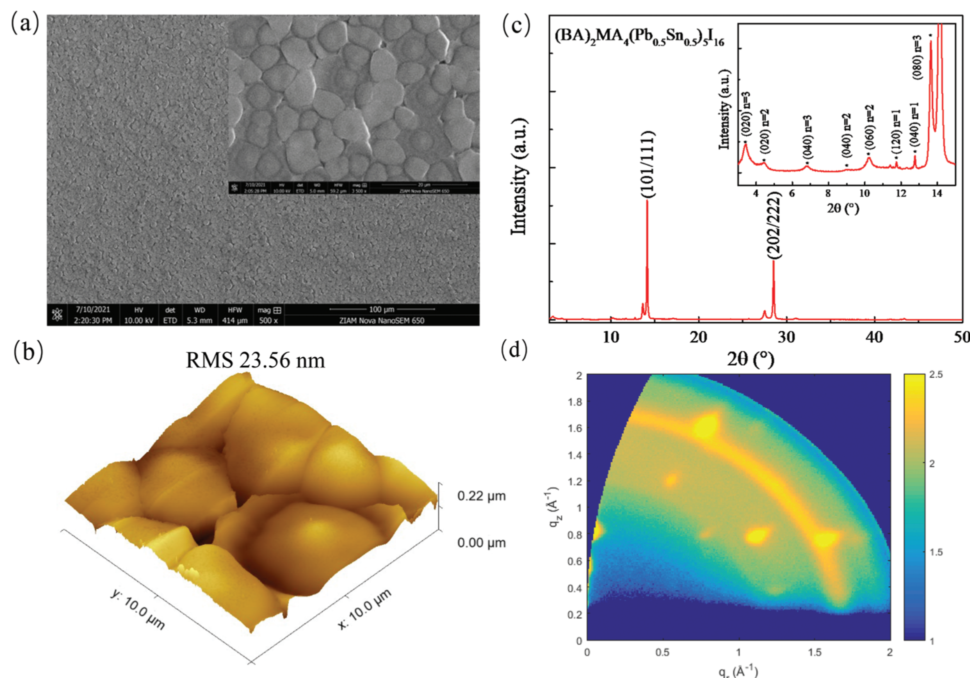

Figure 2. a) SEM image of quasi-2D Pb–Sn perovskite layer. b) AFM image and RMS roughness of the Pb–Sn active layer. c) XRD patterns of the active layer (inserts show an enlargement of diffraction peaks from 3 ° to 15 °). d) GIWAXS patterns of the quasi-2D Pb–Sn thin film.

the Pb–Sn film that could act as traps and hence provide beneficial effects for the RS behavior of our devices. The improved alignment of the crystallites observed by GIWAXS can also play a beneficial role on the performance of the device using the Pb–Sn film.

Good retention and endurance characteristics are vital for reliable memristor operation. **Figure 3**a shows the endurance of quasi-2D Pb–Sn perovskite memory devices, measured by applying continuous write/erase voltage pulses of 2/−2 V for the set/reset process with a read voltage of −0.5 V, which present constant ON/OFF ratio for 2000 switching cycles without degradation, while the pure Sn compound shows large fluctuations in the ON/OFF ratio and degrades over time (Figure S6a, Supporting Information). Typical retention behavior is also monitored at the readout voltage of −0.5 V to confirm the electrical reliability and stability of the device and is reported in Figure 3b. A constant ON/OFF current ratio for quasi-2D Pb–Sn perovskite can be well maintained for more than 2×10^5 s under dark conditions, while only of 4000 s for pure Sn device (Figure S6b, Supporting Information). Figure 3c and Figure S5c (Supporting Information) show the synaptic plasticity reproducibility after application of a series of 200 positive pulses (2 V, 1 s) and 200 negative pulses (−2 V, 1 s) for the Pb–Sn and the Sn-only samples, respectively. For the quasi-2D Pb–Sn perovskite, the synaptic current after five complete potentiation and depression processes are constant over time, showing that our devices exhibit excellent synaptic plasticity and good operational stability. Although Sn-based samples also show synaptic behavior, the peak value of the synaptic current decreases greatly with the increase of the number of cycles (Figure S6c, Supporting Information). In addition, as shown in Figure 3d, the quasi-2D Pb–Sn RS device retains almost the full original bipolar behavior after being stored in glovebox over 3 months, while the switching characteristics of Sn device almost disappear after a week in the same condition due to the easy oxidation of $Sn^{2\pm}$ in $Sn^{4\pm}$ (Figure S7, Supporting Information). In summary, quasi-2D Pb–Sn based memristors show better switching stability and synaptic repeatability, hence for the remaining of the manuscript we continue further characterization of the synaptic behaviors of the quasi-2D Pb–Sn perovskite only.

The synaptic plasticity in the form of STDP plays an important role in achieving neural network functions, here the conductance/synaptic weight variation of memristor are related to the time sequence of the pre- and post-synaptic spikes.[37] Four different forms of STDP are realized by translating the time difference into voltage amplitude differences, as shown in **Figure 4**a–d. The asymmetric Hebbian rule (Figure 4a) is obtained when a pre-synaptic spike is preceding a post-synaptic spike ($\Delta t > 0$, $\Delta t = t_{pre} - t_{post}$) resulting in long-term potentiation (LTP), whereas when a post-synaptic pulse is preceding a pre-synaptic spike ($\Delta t < 0$) leads to long-term depression (LTD), which corresponds with the increase and decrease of conductance (dW) in the quasi-2D Pb–Sn synaptic devices.[38] The square-shaped waveforms of pre-spikes (red color) and post-spikes (blue color) applied on the devices are shown in Figure S8a (Supporting Information). Interestingly, LTP and LTD behavior can also be observed by flipping the input waveforms for asymmetric anti-Hebbian rule (Figure 4b), while the temporal order of the pre- and post-synaptic pulses does not play a role determining symmetric Hebbian rule (Figure 4c) and symmetric anti-Hebbian rule (Figure 4d). The corresponding detailed patterns of the synaptic spikes are shown in Figure S8b–d (Supporting Information). The results confirm that artificial synapses based on quasi-2D Pb–Sn perovskites successfully emulate the STDP functions of biological synapses.

© 2023 The Authors. Small Methods published by Wiley-VCH GmbH

23669608, 2024, 2, Downloaded from https://onlinelibrary.wiley.com/doi/10.1002/smtd.202300040 by Forschungszentrum Jülich GmbH Research Center, Wiley Online Library on [28/01/2025]. See the Terms and Conditions (https://onlinelibrary.wiley.com/terms-and-conditions) on Wiley Online Library for rules of use; OA articles are governed by the applicable Creative Commons License

23669608, 2024, 2, Downloaded from https://onlinelibrary.wiley.com/doi/10.1002/smtd.202300040 by Forschungszentrum Jülich GmbH Research Center, Wiley Online Library on [28/01/2025]. See the Terms and Conditions (https://onlinelibrary.wiley.com/terms-and-conditions) on Wiley Online Library for rules of use; OA articles are governed by the applicable Creative Commons License

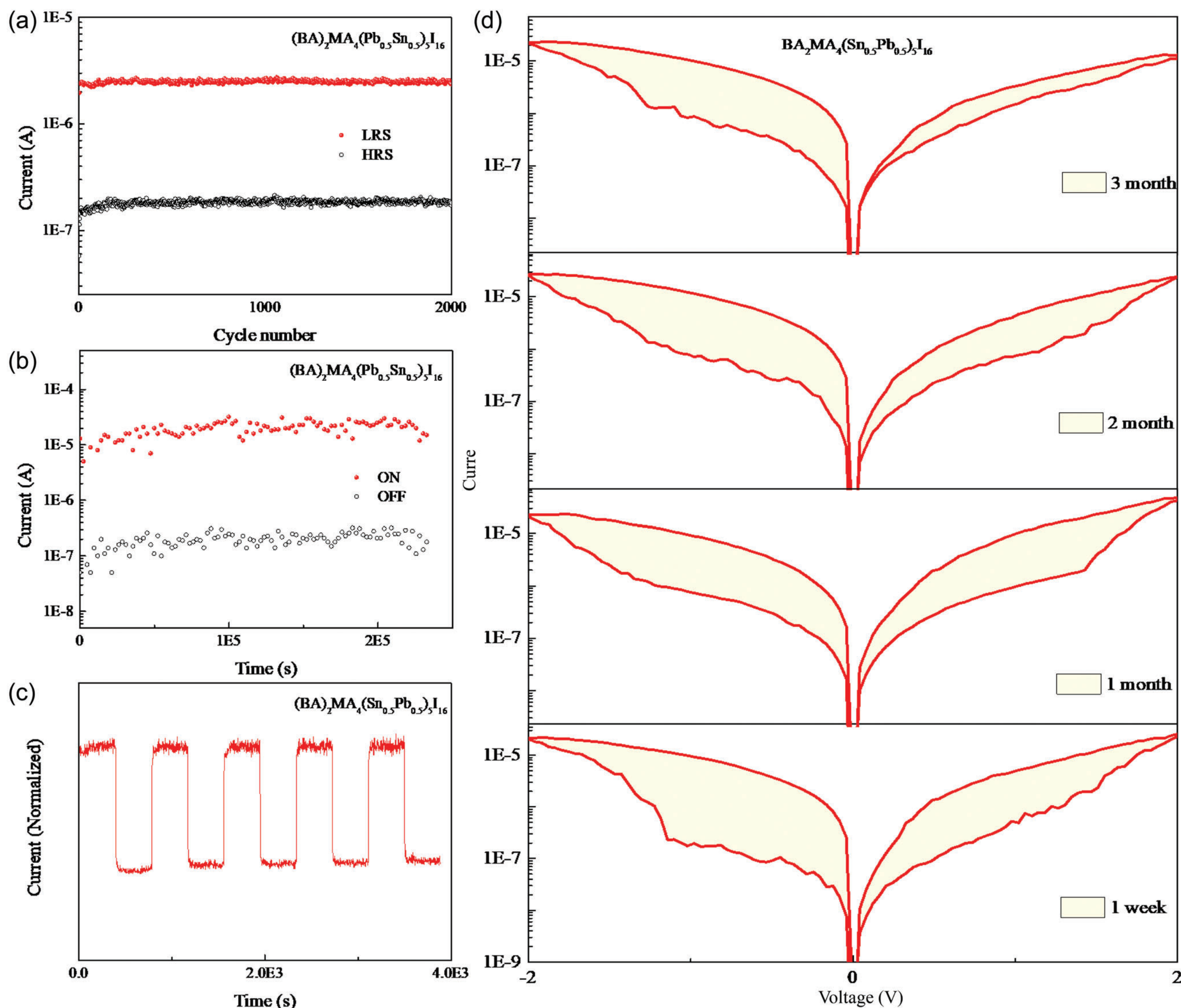

Figure 3. Typical a) endurance and b) retention characteristics of a memory device based on $(BA)_2MA_4(Pb_{0.5}Sn_{0.5})_5I_{16}$. c) Synaptic potentiation and depression behaviors of the quasi-2D Pb–Sn memristive devices. d) Stability tracking of *J*–*V* curves of memory devices based on quasi-2D Pb–Sn compound in a N_2 glovebox.

In addition to the STDP synaptic function, the spiking-rate dependent synaptic plasticity of STP and LTP are also successfully emulated in our memory devices.[17] As shown in Figure 4e, the gradually increasing peak current is induced by a round of 20 identical input pulses with amplitude of 2 V, a width of 1 ms, and interval of 10 ms. However, when the interval is increased to 30 ms, the current increases for the first ten pulses and remains constant for the last ten pulses (Figure S9, Supporting Information). More importantly, the forgetting time of STP gradually increases from 0.28 to 0.47 s with increasing the frequency of stimulation, this indicates that the forgetting rate is decreasing, which is very similar to the memory function of human beings. This may be due to complete charge trapping and de-trapping at defects after a higher number of pulses is applied on the device. Paired-pulse facilitation (PPF) is another synaptic function closely related to STP.[39] As shown in Figure 4f, PPF is observed when two presynaptic spikes with interval time of 20 ms are applied, and the output of the second spike (A2) is larger than that of the first pulse (A1). The trend of PPF can be tracked by the PPF index ((A2–A1)/A1 × 100%), where A1 and A2 represent the peak amplitudes of the first and second pulse responses, respectively. As indicated in the inset picture of Figure 4f and Figure S10 (Supporting Information), the PPF index decreases when the pulse interval increases from 5 to 150 ms, this behavior further proves that our devices have the potential to simulate biological synapses

So far, we have shown the learning behavior of our memristors, but we have not yet commented on the working mechanism of these devices. Log *I*–log *V* characteristics of quasi-2D Sn–Pb memory devices are presented in **Figure 5**a and S11 (Supporting Information), here we fit the curves with the relation $I \propto V^m$, where m can give an indication of the different transport mechanisms.[40] In the HRS state of the set process, the fitting

© 2023 The Authors. Small Methods published by Wiley-VCH GmbH

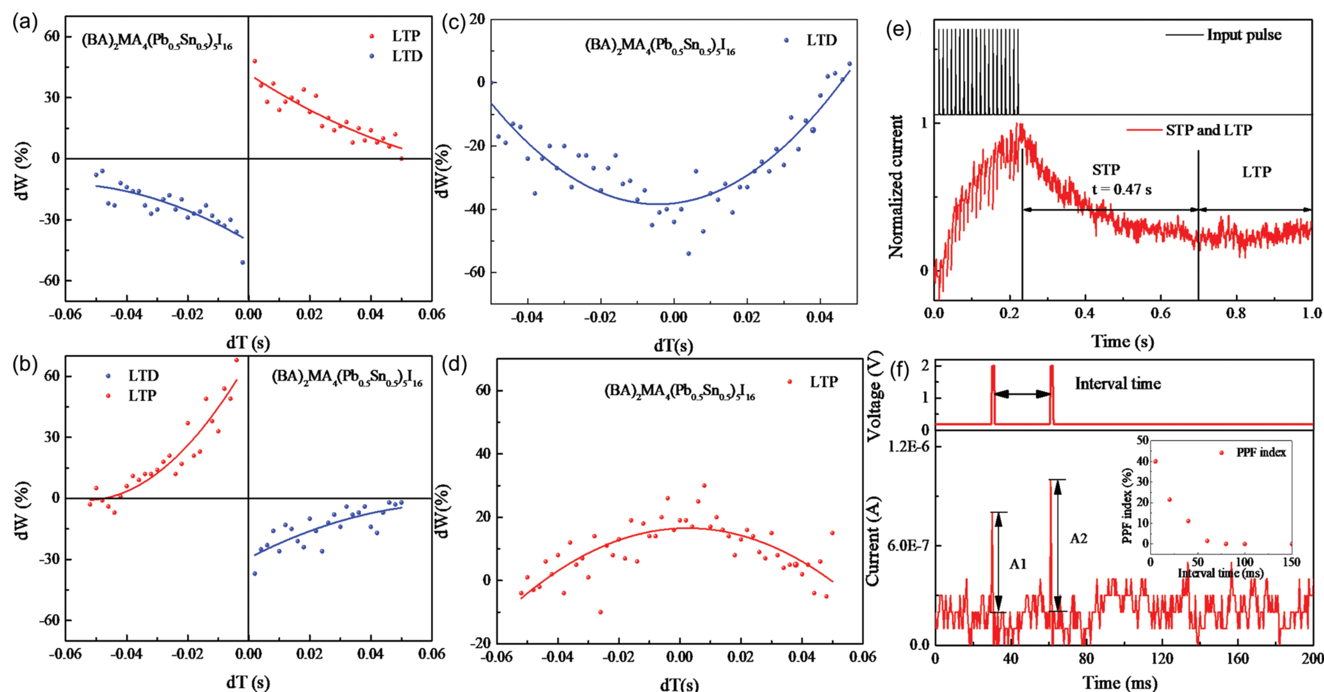

Figure 4. Four different forms of STDP behaviors of $(BA)_2MA_4(Pb_{0.5}Sn_{0.5})_5I_{16}$ based on a) asymmetric Hebbian rule, b) asymmetric anti-Hebbian rule, c) symmetric anti-Hebbian rule, and d) symmetric Hebbian rule. e) STP and LTP curves under continuous 20 pulse stimulation. f) PPF achieved by applying pulse with amplitude of 2 V and interval time of 20 ms, the insert shows the pulse interval dependence of the PPF index.

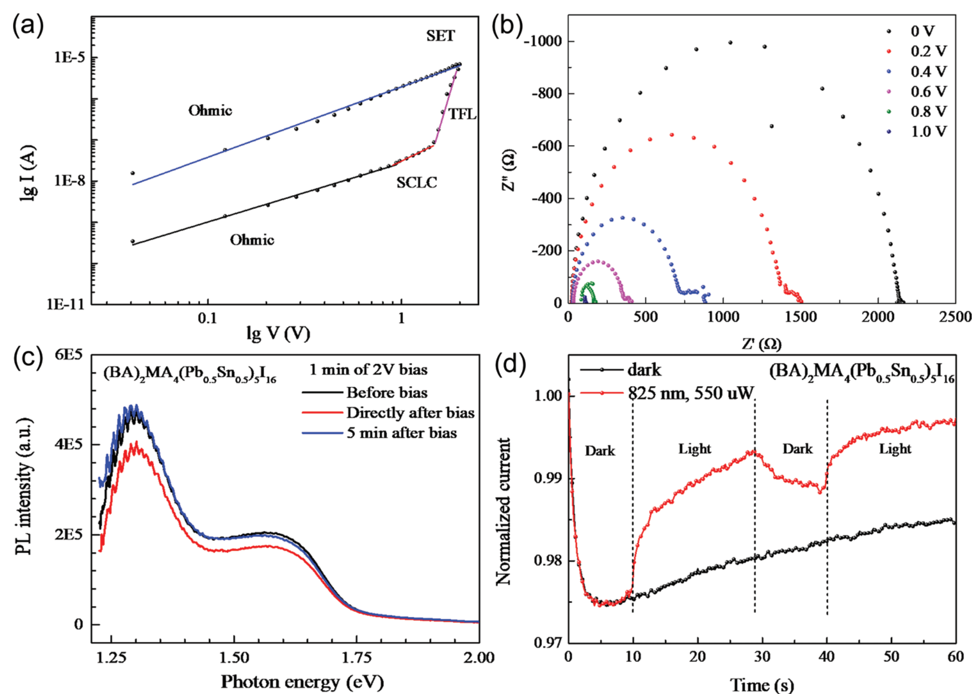

Figure 5. a) Replotted *I–V* characteristics on a double-log scale in set process and their fitting results. b) EIS spectra of qusai-2D Pb–Sn perovskite device at different bias voltages. c) PL intensity of before and after applying a bias of 2 V for 1 min. d) Current response of memory device for quasi-2D Sn–Pb perovskite under dark and illumination conditions.

 © 2023 The Authors. Small Methods published by Wiley-VCH GmbH

23669608, 2024, 2, Downloaded from https://onlinelibrary.wiley.com/doi/10.1002/smtd.202300040 by Forschungszentrum Jülich GmbH Research Center, Wiley Online Library on [28/01/2025]. See the Terms and Conditions (https://onlinelibrary.wiley.com/terms-and-conditions) on Wiley Online Library for rules of use; OA articles are governed by the applicable Creative Commons License

results show that the exponent m has three different values depending on the applied voltage. We observed that the conductive mechanism is transformed from an Ohmic regime (m = 1.12) for the low-voltage region (0–0.86 V) to a shallow-trap space charge limited current (SCLC) regime (m = 2.15) for medium-voltage region (0.86–1.35 V), and then to a trap-filled limited (TFL) SCLC regime (m = 6.15) for higher voltage (1.35–2 V). This behavior suggests that a few injected carriers are trapped by defects (iodine vacancy) in the active layer with increasing voltage, and that trap states limit the current by localizing charge carriers rather than injecting free carriers. As the voltage reaches 1.35 V, all the traps at the specific energy are filled by charge carriers and the device shifts from HRS to LRS. More importantly, migration of the iodine ions is also occurring in this process, indicating a mix slow (ionic) transport and fast (electronic) transport for the RS behavior.[41] During the whole LRS, the linear *I*–*V* curve (m≈1.15) shows Ohmic conduction. The double-logarithm *I*–*V* curve for the negative-voltage stage (reset process) shows similar conductive mechanism as the set process (Figure S11, Supporting Information), which also follows an Ohmic regime (m = 1.14) at 0–0.65 V, a SCLC regime (m -= 2.23) at 0.65–0.86 V, and TFL regime (m = 3.56) at 0.86–2 V. We also perform impedance spectroscopy (EIS) measurements to get deeper insight into the transport mechanism (Figure 5b). The equivalent circuit for fitting the EIS data of quasi-2D Pb–Sn perovskite is present in Figure S12a (Supporting Information), which consists of the series resistance (R_S), the interfacial charge carrier recombination (capacitance C_1 and recombination resistance R_1), the bulk charge carrier recombination (capacitance C_2 and recombination resistance R_2), and a slow process like ionic movement (capacitance C_3 and resistance R_3). The second semicircle is observed at low frequency after applying the bias, which demonstrates a defect state leading to ionic movement in the active layer. The bias dependence of semicircle diameters suggests a strong ionic current contribution under these circumstances, which has a resonance frequency of about 10 kHz. In addition, the irregular EIS curves at high frequency appear when the bias reaches 0.8 V, the real components of the circuit versus frequency are shown in Figure S12b (Supporting Information), which is consistent with the log *I*–log *V* measurements, showing the transitions from Ohmic to SCLC transport.

To better understand the switching mechanism, photoluminescence (PL) spectra of the quasi-2D Sn–Pb perovskite-based device are conducted under bias and various illumination to study the trap states and defects. Figure 5c demonstrates that the PL intensity decreases after applying a bias of 2 V for 1 min, indicating that inherent trap states are formed within the bandgap of the perovskite.[42] The intensity of the PL then completely recovered to its original intensity after 5 min in the dark, showing that traps are healed by migrating ions after removing the bias. A similar dependency is obtained when we extend the bias time to 5 min (Figure S13, Supporting Information), this behavior further illustrates the occurrence of defects-induced charge trapping and de-trapping as well as ionic movement during device operation although it is independent on the minute time scale. It is known that the defects usually act as charge trapping centers creating migration channels for ions,[43] therefore, we designed an experiment to investigate if we could de-trap the charges using a laser as excitation source. The current response both with and without 825 nm wavelength laser light illumination under a bias of 0.8 V is shown in Figure 5d. We split the measurement into alternating dark and light intervals. Upon laser exposure, the current of the memory device sharply increases, indicating the generation of photocurrent and simultaneously trap filling by these photo-generated charge carriers.[44] When the laser light is blocked at the 28th second, the current drops as is expected with the absence of the photo-generated charges. Interestingly, the current does not reach the same value as when the device was measured in the dark. Thus, the laser exposure introduced a new equilibrium of traps, which shows a reversible dynamic that is longer than the second time scale probed here. We also investigated the current response with shorter wavelength of 560 nm (131 uW) and longer wavelength of 975 nm (1200 uW) and 1100 nm (2200 uW), as show in Figure S14 (Supporting Information), A similar current response is obtained at a wavelength of 560 nm, however, the current response is poor at a wavelength of 975 nm and there is almost no response at an illumination of 1100 nm, which highlights the importance of band-to-band transition in the passivation of defects.[45] The results also show that defects are the main source of device RS characteristics.

3. Conclusion

In summary, we have successfully fabricated RS memory devices based on quasi-2D Pb–Sn mixed perovskites with the scalable blade coating technique. The mixed Pb–Sn devices show memory characteristics without any forming process, furthermore, they show excellent endurance (2000 cycles), retention (10^5 s), storage stability (3 months), and synaptic behaviors (STDP, PPF, STP and LTP). Furthermore, by correlating the results of SCLC, EIS, and PL measurements, we show that a mix of slow (ionic) transport and fast (electronic) transport (charge trapping and de-trapping) are responsible for the resistive switching. This study paves the way for developing more environmentally friendly and robust quasi-2D perovskite memory devices with scalable deposition methods.

Supporting Information

Supporting Information is available from the Wiley Online Library or from the author.

Acknowledgements

The authors thank the kind technical support of Arjen Kamp, Teo Zaharia, and David Garcia Romero. The authors also would like to acknowledge the financial support of the CogniGron Research Center. This work was partially financed through the Materials for Sustainability (Mat4Sus) program (Grant no. 739.017.005) of the Netherlands Organisation for Scientific Research (NWO). L.C. acknowledges the China Scholarship Council. J.X. would like to acknowledge the National Natural Science Foundation of China (Grant no. 62205264), and Xi'an Jiaotong University Young Talents Support Program (Grant no. 11302291010704).

Conflict of Interest

The authors declare no conflict of interest.

© 2023 The Authors. Small Methods published by Wiley-VCH GmbH

23669608, 2024, 2, Downloaded from https://onlinelibrary.wiley.com/doi/10.1002/smtd.202300040 by Forschungszentrum Jülich GmbH Research Center, Wiley Online Library on [28/01/2025]. See the Terms and Conditions (https://onlinelibrary.wiley.com/terms-and-conditions) on Wiley Online Library for rules of use; OA articles are governed by the applicable Creative Commons License

Data Availability Statement

The data that support the findings of this study are available from the corresponding author upon reasonable request.

Keywords

blade coating, charge trapping and de-trapping, ionic movements, quasi-2D Pb–Sn perovskite, synaptic plasticity

Received: January 9, 2023
Revised: April 24, 2023
Published online: June 7, 2023

[1] S. Gao, X. Yi, J. Shang, G. Liu, R. W. Li, *Chem. Soc. Rev.* **2019**, *48*, 1531.
[2] J. Zhu, T. Zhang, Y. Yang, R. Huang, *Appl. Phys. Rev.* **2020**, *7*, 011312.
[3] Y. Li, Z. Wang, R. Midya, Q. Xia, J. J. Yang, *J. Phys. D: Appl. Phys.* **2018**, *51*, 503002.
[4] Z. Lv, Y. Wang, J. Chen, J. Wang, Y. Zhou, S.-T. Han, *Chem. Rev.* **2020**, *120*, 3941.
[5] B. Li, W. Hui, X. Ran, Y. Xia, F. Xia, L. Chao, Y. Chen, W. Huang, *J. Mater. Chem. C* **2019**, *7*, 7476.
[6] J. Choi, J. S. Han, K. Hong, S. Y. Kim, H. W. Jang, *Adv. Mater.* **2018**, *30*, 1704002.
[7] S. M. Hus, R. Ge, P. A. Chen, L. Liang, G. E. Donnelly, W. Ko, F. Huang, M. H. Chiang, A. P. Li, D. Akinwande, *Nat. Nanotechnol.* **2021**, *16*, 58.
[8] T. Zhang, C. Hu, S. Yang, *Small Methods* **2019**, *4*, 1900552.
[9] K. Yan, B. Dong, X. Xiao, S. Chen, B. Chen, X. Gao, H. Hu, W. Wen, J. Zhou, D. Zou, *Sci. Rep.* **2017**, *7*, 6025.
[10] A. A. Zhumekenov, M. I. Saidaminov, O. F. Mohammed, O. M. Bakr, *Joule* **2021**, *5*, 2027.
[11] X. Zhao, Z. Wang, W. Li, S. Sun, H. Xu, P. Zhou, J. Xu, Y. Lin, Y. Liu, *Adv. Funct. Mater.* **2020**, *30*, 1910151.
[12] Q. Liu, S. Gao, L. Xu, W. Yue, C. Zhang, H. Kan, Y. Li, G. Shen, *Chem. Soc. Rev.* **2022**, *51*, 3341.
[13] Y. Shao, Y. Fang, T. Li, Q. Wang, Q. Dong, Y. Deng, Y. Yuan, H. Wei, M. Wang, A. Gruverman, J. Shield, J. Huang, *Energy Environ. Sci.* **2016**, *9*, 1752.
[14] J. S. Han, Q. Van Le, J. Choi, K. Hong, C. W. Moon, B.-S. Kim, B.-S. Kim, B.-S. Kim, H. W. Jang, *Adv. Funct. Mater.* **2018**, *28*, 1705783.
[15] Y. Wang, Z. Lv, Q. Liao, H. Shan, J. Chen, Y. Zhou, L. Zhou, X. Chen, V. A. L. Roy, Z. Wang, Z. Xu, Y.-J. Zeng, S.-T. Han, *Adv. Mater.* **2018**, *30*, 1800327.
[16] X. F. Cheng, W. H. Qian, J. Wang, C. Yu, J. H. He, H. Li, Q. F. Xu, D. Y. Chen, N. J. Li, J. M. Lu, *Small* **2019**, *15*, 1905731.
[17] H. Tian, L. Zhao, X. Wang, Y.-W. Yeh, N. Yao, B. P. Rand, T.-L. Ren, *ACS Nano* **2017**, *11*, 12247.
[18] R. A. John, Y. Demirag, Y. Shynkarenko, Y. Berezovska, N. Ohannessian, M. Payvand, P. Zeng, M. I. Bodnarchuk, F. Krumeich, G. Kara, I. Shorubalko, M. V. Nair, G. A. Cooke, T. Lippert, G. Indiveri, M. V. Kovalenko, *Nat. Commun.* **2022**, *13*, 2074.
[19] M. Kumar, H.-S. Kim, D. Y. Park, M. S. Jeong, J. Kim, *ACS Appl. Mater. Interfaces* **2018**, *10*, 12768.
[20] X. Li, J. M. Hoffman, M. G. Kanatzidis, *Chem. Rev.* **2021**, *121*, 2230.
[21] J. Xi, I. Spanopoulos, K. Bang, J. Xu, H. Dong, Y. Yang, C. D. Malliakas, J. M. Hoffman, M. G. Kanatzidis, Z. Wu, *J. Am. Chem. Soc.* **2020**, *142*, 19705.
[22] A. Solanki, A. Guerrero, Q. Zhang, J. Bisquert, T. C. Sum, *J. Phys. Chem. Lett.* **2019**, *11*, 463.
[23] J.-Y. Seo, J. Choi, H.-S. Kim, J. Kim, J.-M. Yang, C. Cuhadar, J. S. Han, S.-J. Kim, D. Lee, H. W. Jang, N.-G. Park, *Nanoscale* **2017**, *9*, 15278.
[24] H. Kim, M.-J. Choi, J. M. Suh, J. S. Han, S. G. Kim, Q. V. Le, S. Y. Kim, H. W. Jang, *NPG Asia Mater.* **2020**, *12*, 21.
[25] S. J. Kim, T. H. Lee, J.-M. Yang, J. W. Yang, Y. J. Lee, M.-J. Choi, S. A. Lee, J. M. Suh, K. J. Kwak, J. H. Baek, I. H. Im, D. E. Lee, J. Y. Kim, J. Kim, J. S. Han, S. Y. Kim, D. Lee, N.-G. Park, H. W. Jang, *Mater. Today* **2022**, *52*, 19.
[26] K. J. Kwak, D. E. Lee, S. J. Kim, H. W. Jang, *J. Phys. Chem. Lett.* **2021**, *12*, 8999.
[27] Y. Fang, S. Zhai, L. Chu, J. Zhong, *ACS Appl. Mater. Interfaces* **2021**, *13*, 17141.
[28] X. Xiao, J. Hu, S. Tang, K. Yan, B. Gao, H. Chen, D. Zou, *Adv. Mater. Technol.* **2020**, *5*, 1900914.
[29] C. Cuhadar, S.-G. Kim, J.-M. Yang, J.-Y. Seo, D. Lee, N.-G. Park, *ACS Appl. Mater. Interfaces* **2018**, *10*, 29741.
[30] J.-M. Yang, E.-S. Choi, S.-Y. Kim, J.-H. Kim, J.-H. Park, N.-G. Park, *Nanoscale* **2019**, *11*, 6453.
[31] F. Zeng, Y. Guo, W. Hu, Y. Tan, X. Zhang, J. Feng, X. Tang, *ACS Appl. Mater. Interfaces* **2020**, *12*, 23094.
[32] J. Xi, M. A. Loi, *ACS Energy Lett.* **2021**, *6*, 1803.
[33] B. Hwang, J.-S. Lee, *Adv. Mater.* **2017**, *29*, 1701048.
[34] J. Xi, H. Duim, M. Pitaro, K. Gahlot, J. Dong, G. Portale, M. A. Loi, *Adv. Funct. Mater.* **2021**, *31*, 2105734.
[35] C. C. Stoumpos, C. D. Malliakas, M. G. Kanatzidis, *Inorg. Chem.* **2013**, *52*, 9019.
[36] C. C. Stoumpos, L. Mao, C. D. Malliakas, M. G. Kanatzidis, *Inorg. Chem.* **2017**, *56*, 56.
[37] R. A. John, N. Yantara, Y. F. Ng, G. Narasimman, E. Mosconi, D. Meggiolaro, M. R. Kulkarni, P. K. Gopalakrishnan, C. A. Nguyen, F. De Angelis, S. G. Mhaisalkar, A. Basu, N. Mathews, *Adv. Mater.* **2018**, *30*, 1805454.
[38] Z. Xiao, J. Huang, *Adv. Electron. Mater.* **2016**, *2*, 1600100.
[39] L. Hu, S. Fu, Y. Chen, H. Cao, L. Liang, H. Zhang, J. Gao, J. Wang, F. Zhuge, *Adv. Mater.* **2017**, *29*, 1606927.
[40] M. J. Speirs, D. N. Dirin, M. Abdu-Aguye, D. M. Balazs, M. V. Kovalenko, M. A. Loi, *Energy Environ. Sci.* **2016**, *9*, 2916.
[41] Z. Xiong, W. Hu, Y. She, Q. Lin, L. Hu, X. Tang, K. Sun, *ACS Appl. Mater. Interfaces* **2019**, *11*, 30037.
[42] Y. C. Zhao, W. K. Zhou, X. Zhou, K. H. Liu, D. P. Yu, Q. Zhao, *Light: Sci. Appl.* **2017**, *6*, e16243.
[43] X. Zhu, J. Lee, W. D. Lu, *Adv. Mater.* **2017**, *29*, 1700527.
[44] X. Guan, W. Hu, M. A. Haque, N. Wei, Z. Liu, A. Chen, T. Wu, *Adv. Funct. Mater.* **2018**, *28*, 1704665.
[45] H.-H. Fang, F. Wang, S. Adjokatse, N. Zhao, M. A. Loi, *Adv. Funct. Mater.* **2016**, *26*, 4653.

© 2023 The Authors. Small Methods published by Wiley-VCH GmbH

23669608, 2024, 2, Downloaded from https://onlinelibrary.wiley.com/doi/10.1002/smtd.202300040 by Forschungszentrum Jülich GmbH Research Center, Wiley Online Library on [28/01/2025]. See the Terms and Conditions (https://onlinelibrary.wiley.com/terms-and-conditions) on Wiley Online Library for rules of use; OA articles are governed by the applicable Creative Commons License